

Supporting Information

Porous Metal–Organic Frameworks with Lewis Basic Nitrogen Sites for High-Capacity Methane Storage

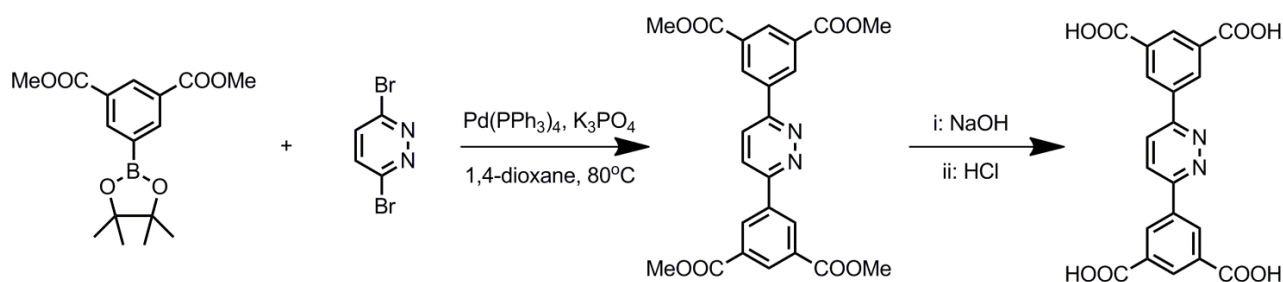
Bin Li,^a Hui-Min Wen,^a Hailong Wang,^a Hui Wu,^b Taner Yildirim,^{b,c} Wei Zhou,^{*b} and Banglin Chen^{*a}

^a *Department of Chemistry, University of Texas at San Antonio, One UTSA Circle, San Antonio, Texas 78249-0698, USA. Fax: (+1)-210-458-7428; E-mail: banglin.chen@utsa.edu*

^b *NIST Center for Neutron Research, National Institute of Standards and Technology, Gaithersburg, Maryland 20899-6102, United States. E-mail: wzhou@nist.gov*

^c *Department of Materials Science and Engineering, University of Pennsylvania, Philadelphia, Pennsylvania 19104-6272, United States*

Scheme S1. Synthetic routes to the organic linker H₄L3.



Tetramethyl 5, 5'-(pyridazine-2, 5-diyl)diisophthalate. 2, 5-Dibromopyridazine (1.18 g, 5 mmol), 5-(4,4,5,5-tetramethyl-1,3,2-dioxaborolan-2-yl) isophthalate (3.52 g, 11 mmol), K₃PO₄ (2.55g, 12 mmol) and tetrakis(triphenylphosphine) palladium(0) (0.3 g, 0.26 mmol) were dissolved in dry 1,4-dioxane (80 mL) under N₂ atmosphere. The mixture was stirred at 80 °C for two days. After that, the precipitate was collected by filtration, and washed with 1, 4-dioxane to obtain the pure product. Yield: 50% (1.16 g). ¹H NMR (500 MHz, CDCl₃, ppm): δ 9.05 (s, 4H), 8.84 (s, 2H), 8.15 (s, 2H), 4.01 (s, 12H).

5, 5'-(pyridazine-2, 5-diyl)diisophthalic acid (H₄L3). Tetramethyl 5, 5'-(pyridazine-2, 5-diyl)diisophthalate (1.16 g, 2.5 mmol) was suspended in 50 mL THF, and then a 2M KOH aqueous solution (75 mL) was added. The mixture was stirred at 60 °C overnight until it became clear. After that THF was removed under reduced pressure and dilute HCl was then added to the remaining aqueous solution to acidify PH = 2. The precipitate was collected by filtration, washed with water for several times, and dried to afford white powder. Yield: 0.97 g (95%). ¹H NMR (500 MHz, d⁶-DMSO, ppm): δ = 13.62 (s, 4H), 8.95 (s, 4H), 8.60 (s, 2H), 8.51 (s, 2H). ¹³C NMR (d⁶-DMSO, ppm): δ = 167.00, 156.73, 137.07, 133.03, 131.89, 131.84, 125.95.

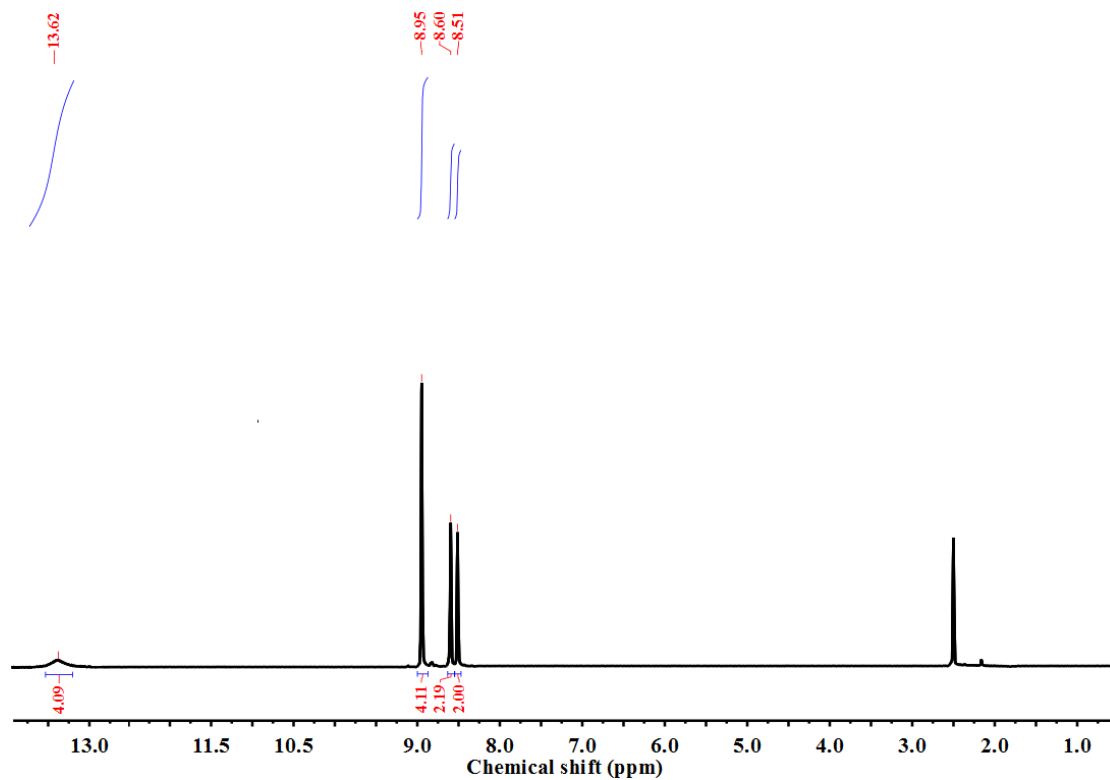


Figure S1. ^1H (DMSO- d_6 , 500MHz) spectra of the ligand $\text{H}_4\text{L3}$.

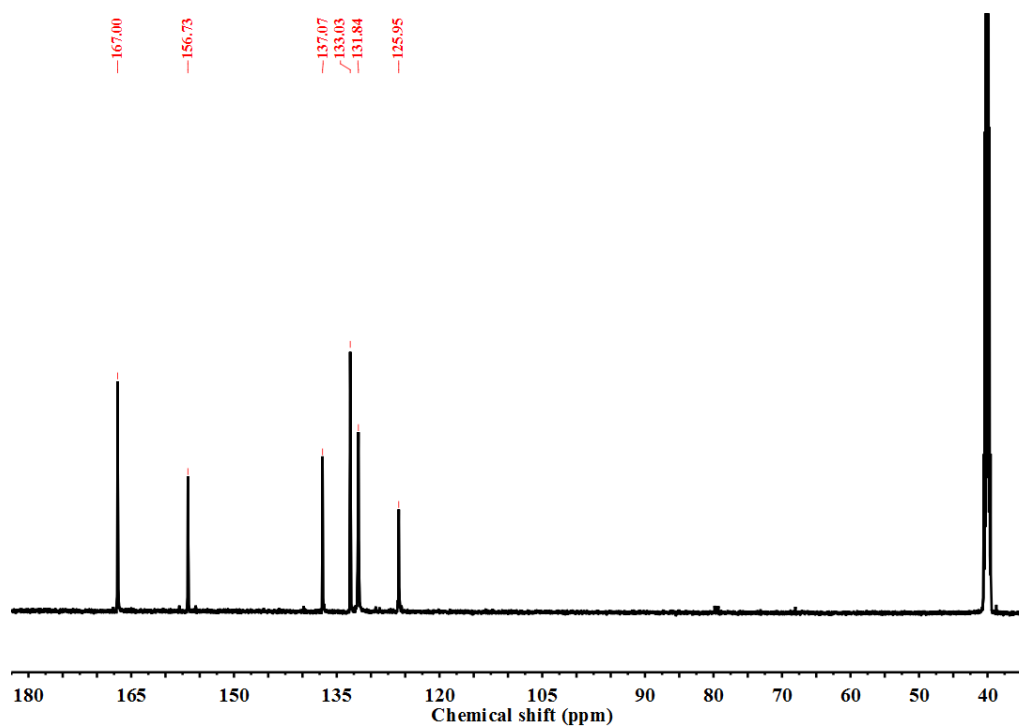


Figure S2. ^{13}C (DMSO- d_6 , 500MHz) spectra of the ligand $\text{H}_4\text{L3}$.

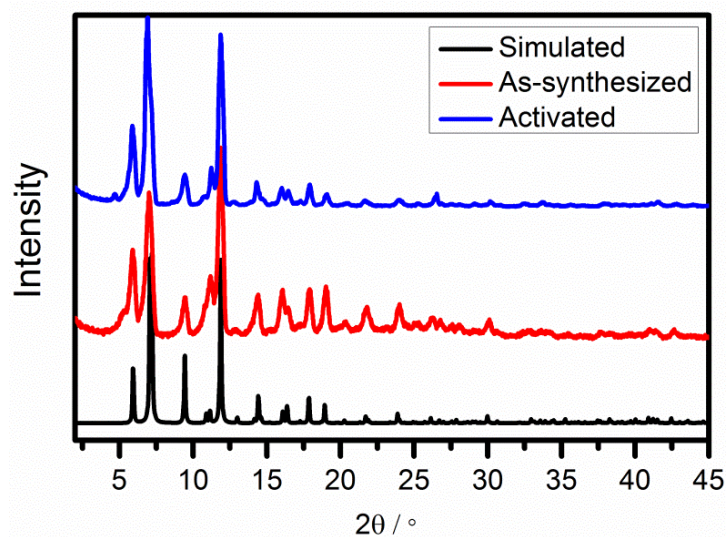


Figure S3. PXRD patterns of as-synthesized UTSA-75 (red) and activated UTSA-75a (blue) along with the simulated XRD pattern from the single-crystal X-ray structure (black).

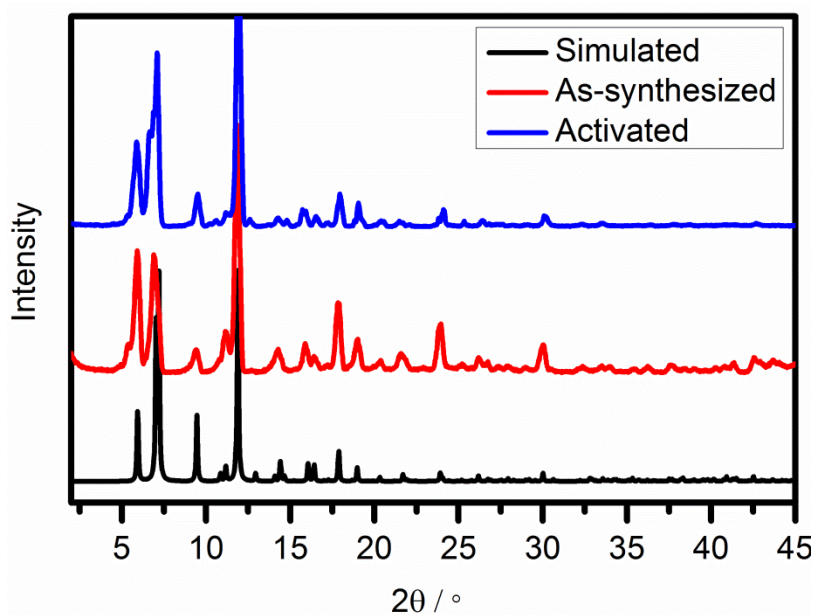


Figure S4. PXRD patterns of as-synthesized ZJU-5 (red) and activated ZJU-5a (blue) along with the simulated XRD pattern from the single-crystal X-ray structure (black).

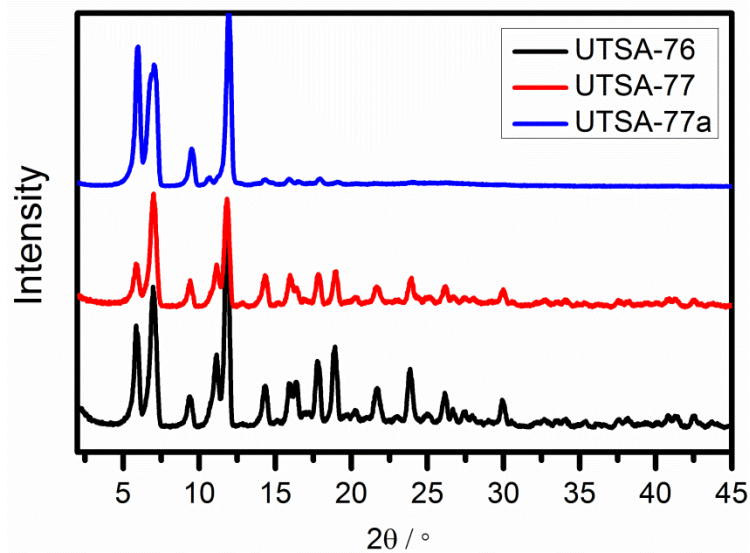


Figure S5. PXRD patterns of as-synthesized UTSA-77 (red) and activated UTSA-77a (blue) along with the XRD pattern of as-synthesized UTSA-76 (black).

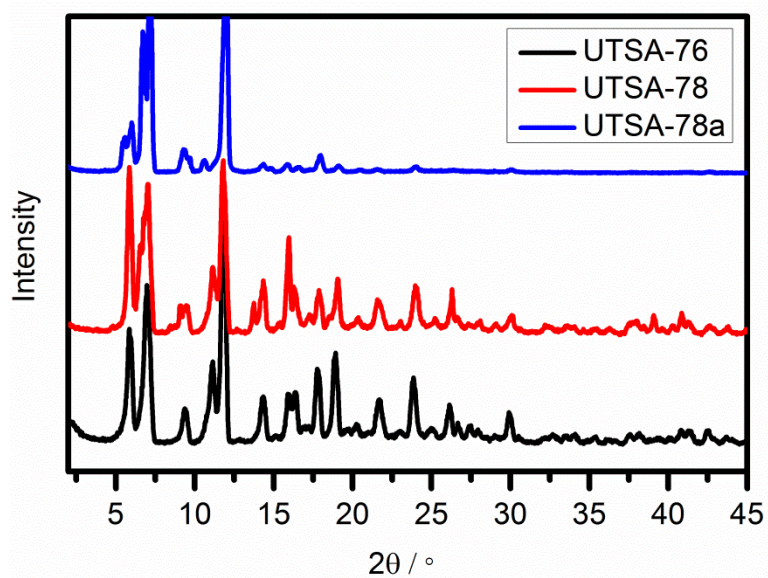


Figure S6. PXRD patterns of as-synthesized UTSA-78 (red) and activated UTSA-78a (blue) along with the XRD pattern of as-synthesized UTSA-76 (black).

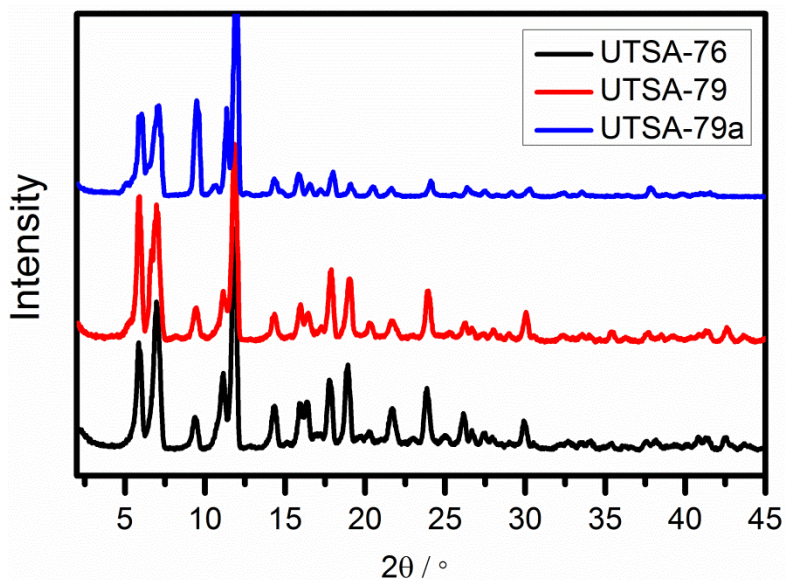


Figure S7. PXRD patterns of as-synthesized UTSA-79 (red) and activated UTSA-79a (blue) along with the XRD pattern of as-synthesized UTSA-76 (black).

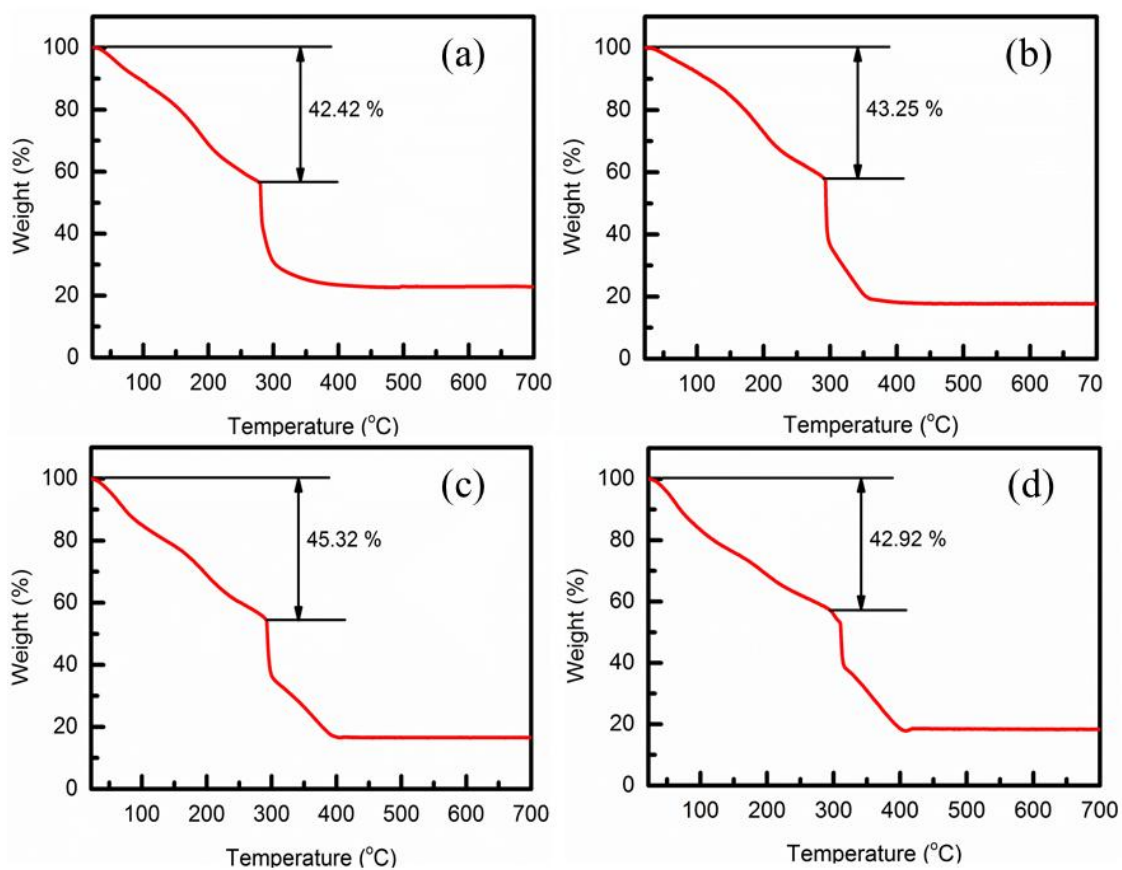


Figure S8. TGA curves of as-synthesized (a) UTSA-75; (b) UTSA-77; (c) UTSA-78; (d) UTSA-79.

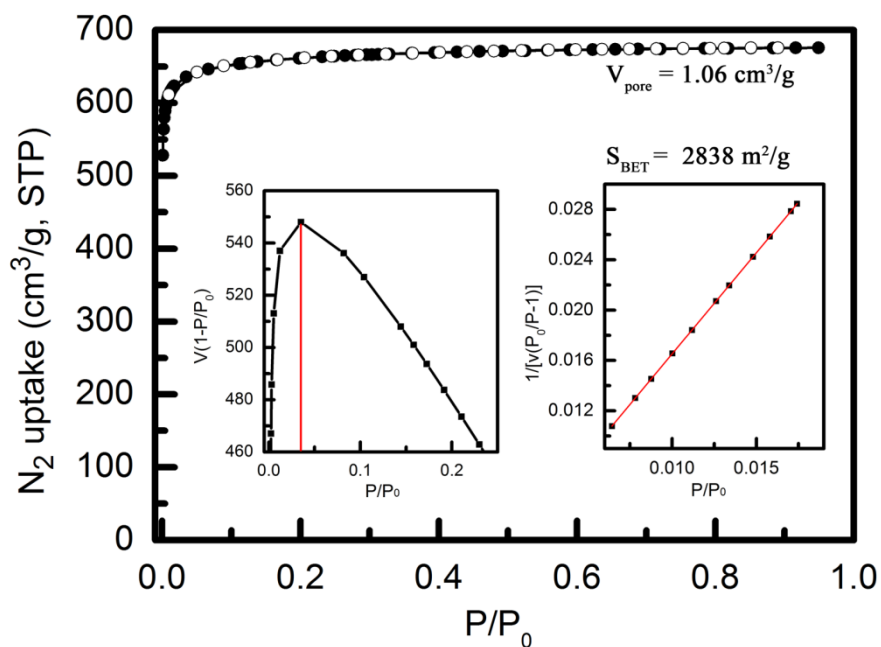


Figure S9. Nitrogen isotherm at 77 K with consistency and BET plots for the activated UTSA-75a sample.

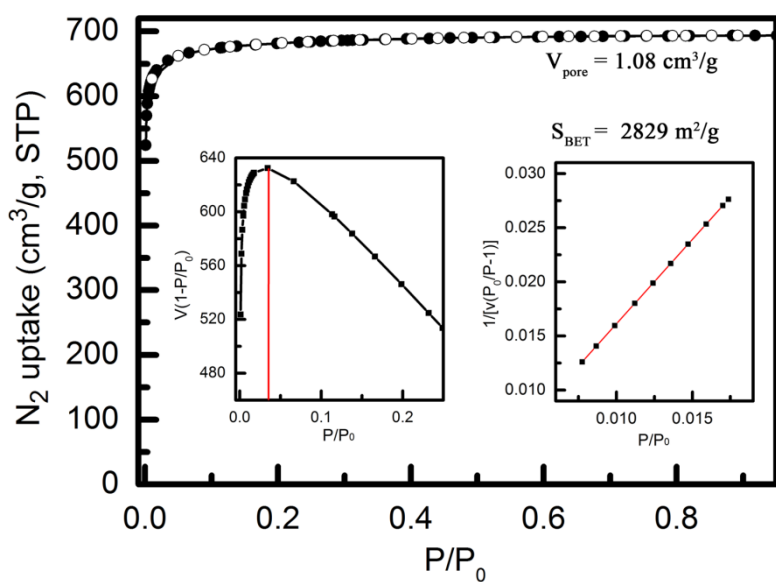


Figure S10. Nitrogen isotherm at 77 K with consistency and BET plots for the activated ZJU-5a sample.

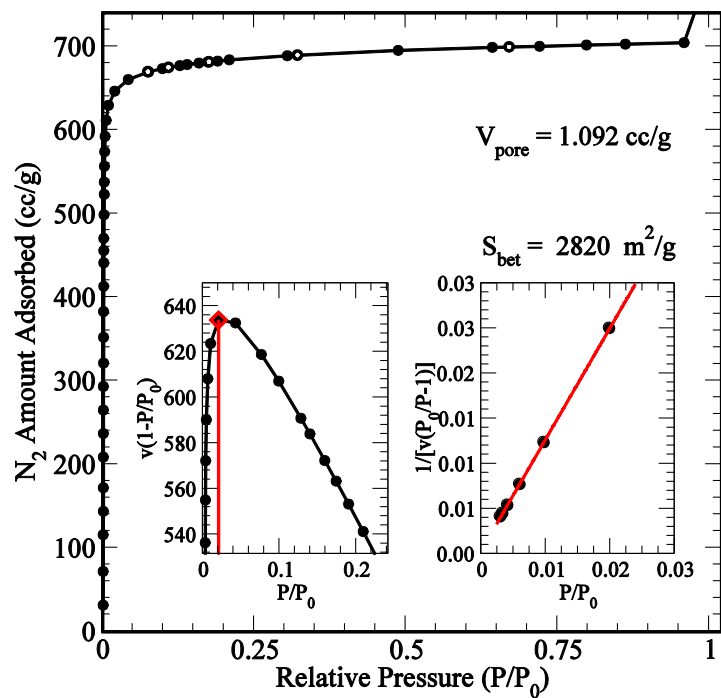


Figure S11. Nitrogen isotherm at 77 K with consistency and BET plots for the activated UTSA-76a sample.

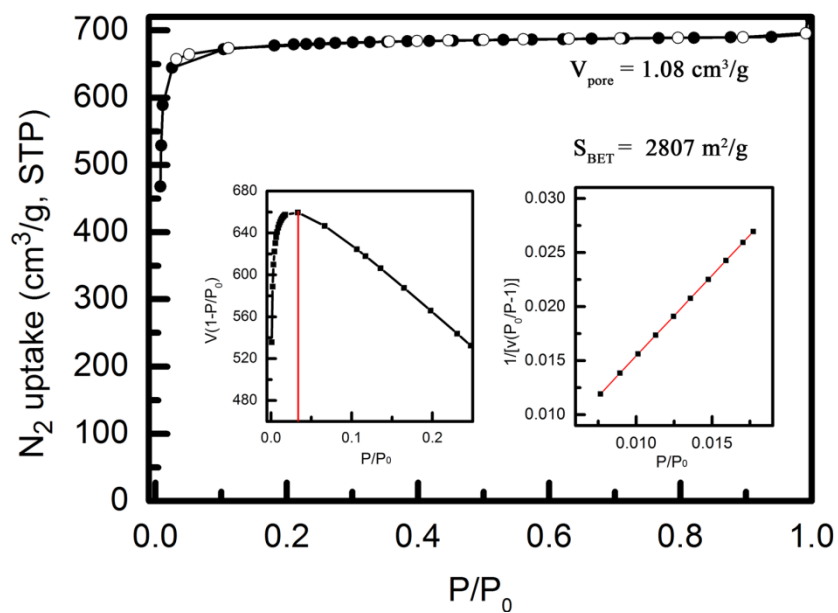


Figure S12. Nitrogen isotherm at 77 K with consistency and BET plots for the activated UTSA-77a sample.

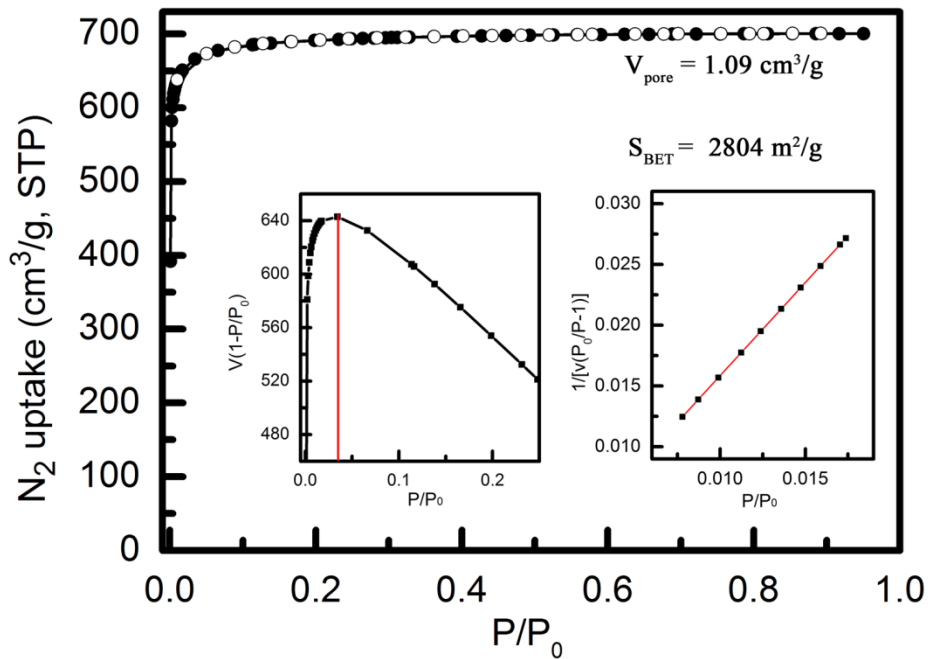


Figure S13. Nitrogen isotherm at 77 K with consistency and BET plots for the activated UTSA-78a sample.

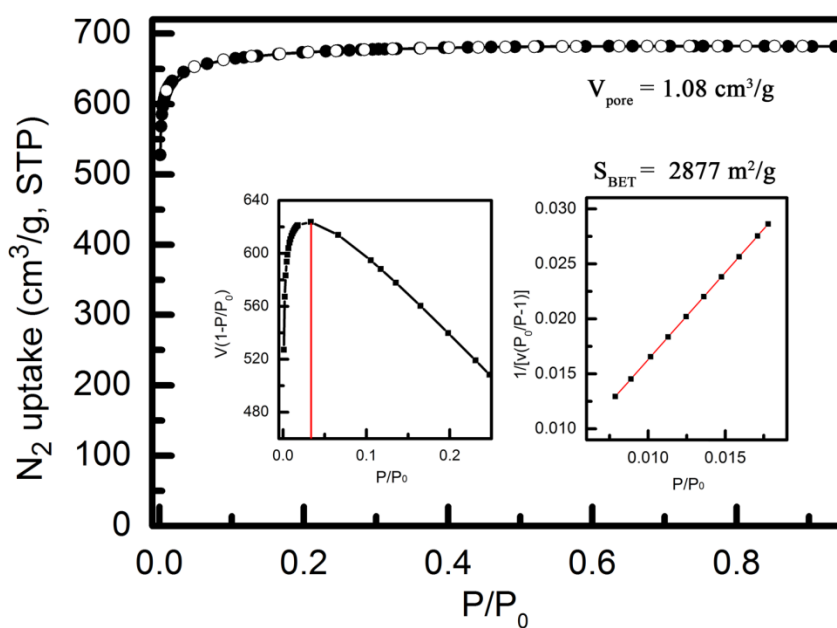


Figure S14. Nitrogen isotherm at 77 K with consistency and BET plots for the activated UTSA-79a sample.

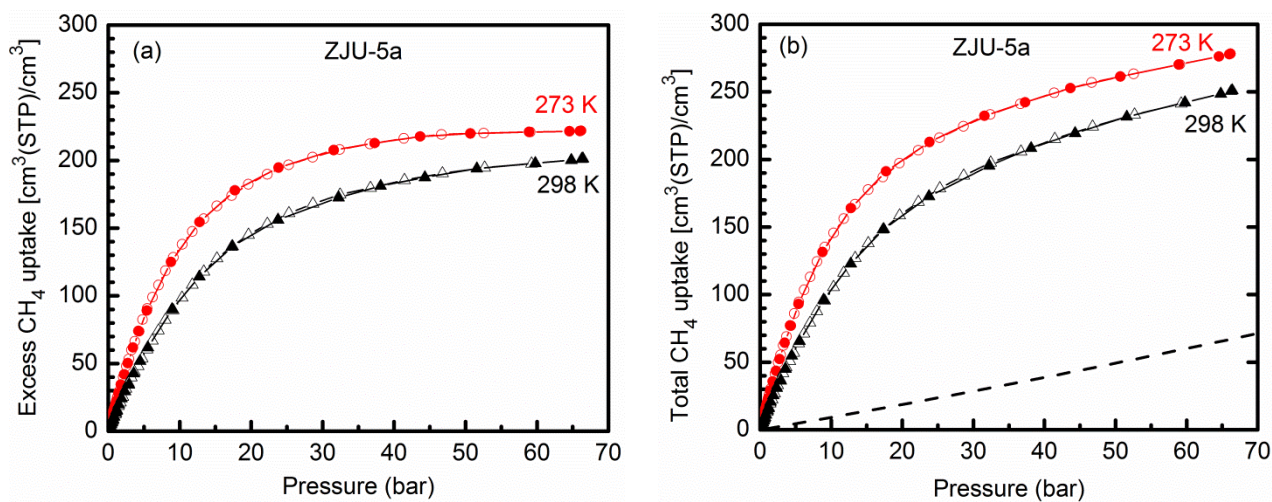


Figure S15. Excess (a) and total (b) high-pressure methane sorption isotherms of ZJU-5a at 273 K (red) and 298 K (black). The filled and open symbols represent adsorption and desorption, respectively. For comparison, data of pure methane gas stored in a high pressure gas tank is represented as black line in (b). The adsorption data have an estimated standard deviation of $\sim 1\%$.¹

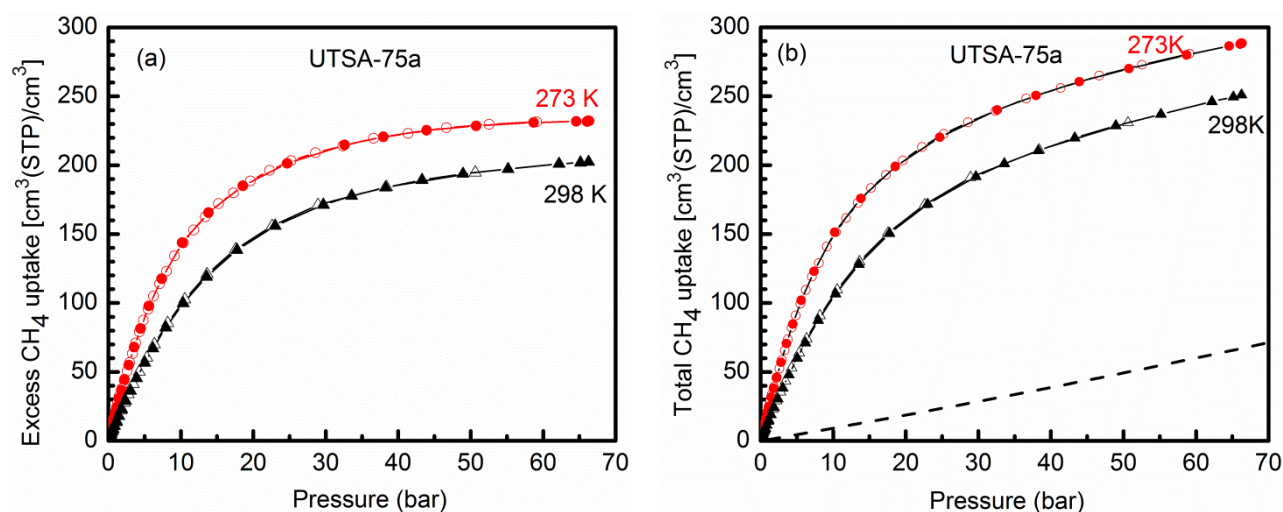


Figure S16. Excess (a) and total (b) high-pressure methane sorption isotherms of UTSA-75a at 273 K (red) and 298 K (black). The filled and open symbols represent adsorption and desorption, respectively. For comparison, data of pure methane gas stored in a high pressure gas tank is represented as black line in (b).

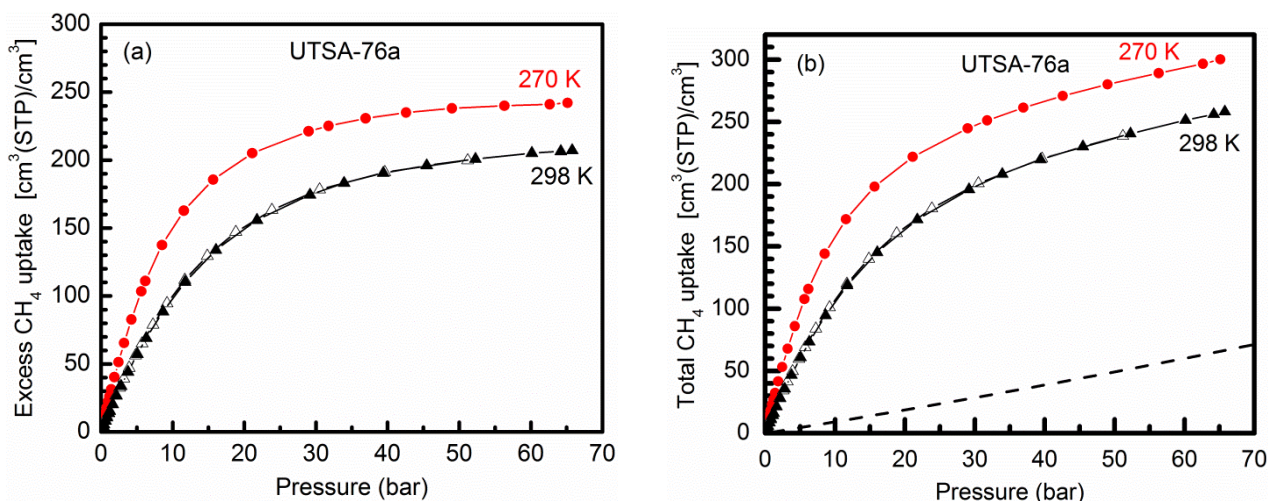


Figure S17. Excess (a) and total (b) high-pressure methane sorption isotherms of UTSA-76a at 273 K (red) and 298 K (black). The filled and open symbols represent adsorption and desorption, respectively. For comparison, data of pure methane gas stored in a high pressure gas tank is represented as black line in (b).

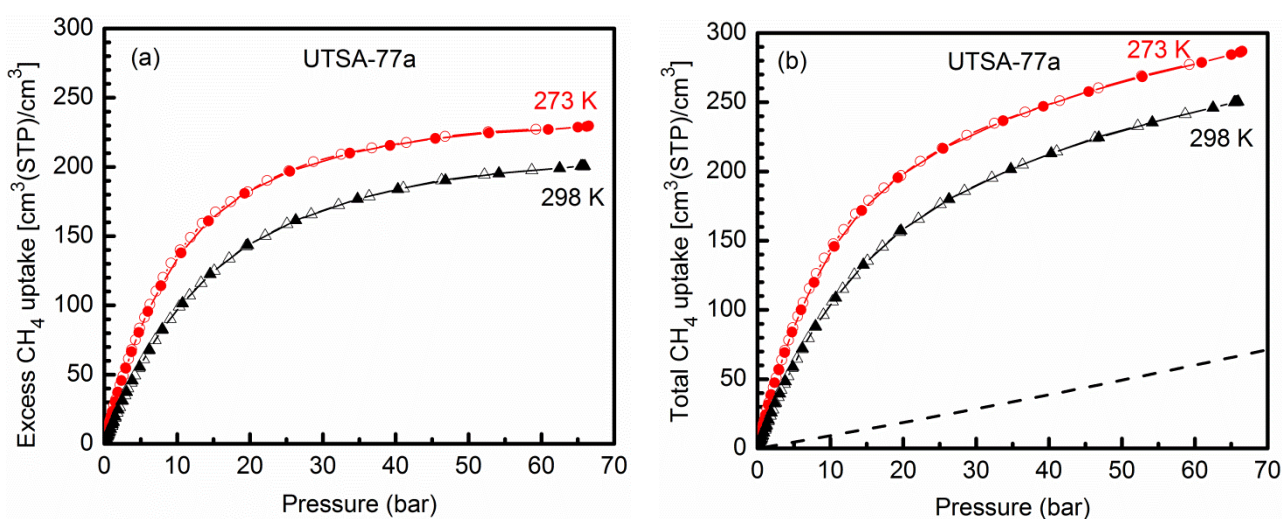


Figure S18. Excess (a) and total (b) high-pressure methane sorption isotherms of UTSA-77a at 273 K (red) and 298 K (black). The filled and open symbols represent adsorption and desorption, respectively. For comparison, data of pure methane gas stored in a high pressure gas tank is represented as black line in (b).

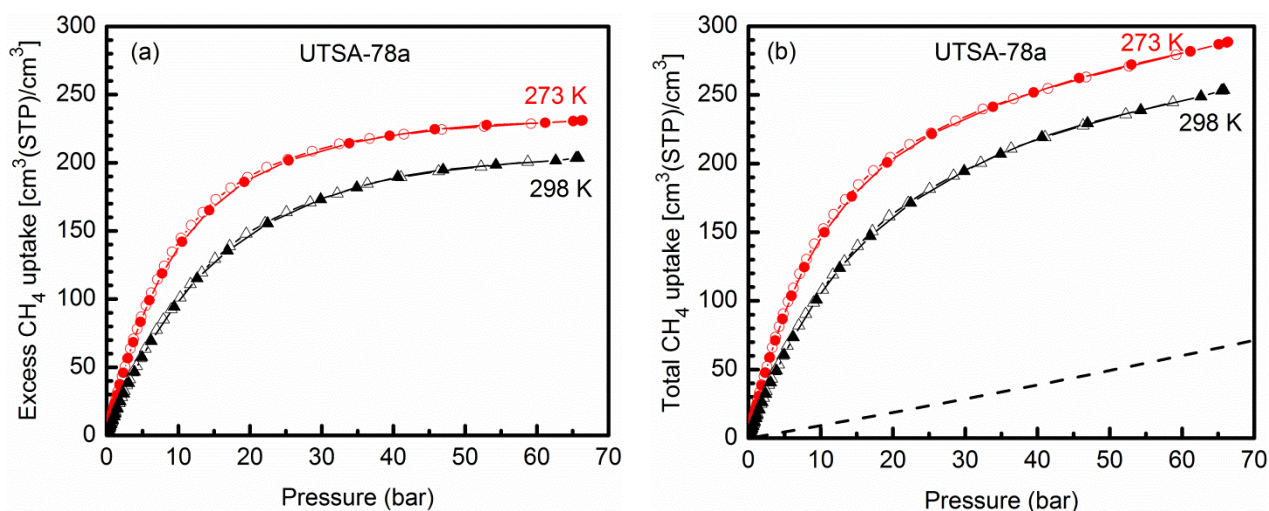


Figure S19. Excess (a) and total (b) high-pressure methane sorption isotherms of UTSA-78a at 273 K (red) and 298 K (black). The filled and open symbols represent adsorption and desorption, respectively. For comparison, data of pure methane gas stored in a high pressure gas tank is represented as black line in (b).

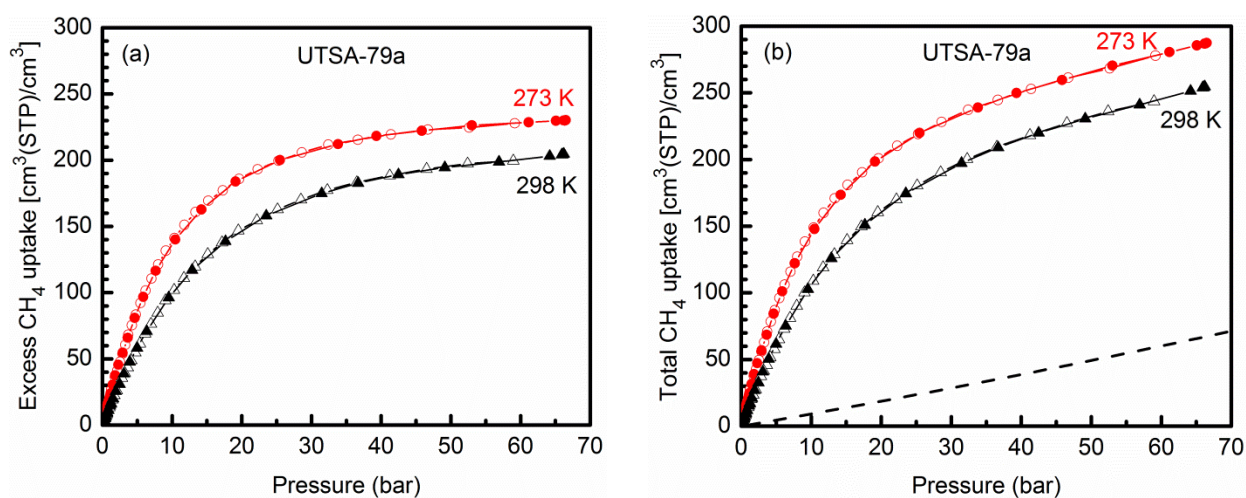


Figure S20. Excess (a) and total (b) high-pressure methane sorption isotherms of UTSA-79a at 273 K (red) and 298 K (black). The filled and open symbols represent adsorption and desorption, respectively. For comparison, data of pure methane gas stored in a high pressure gas tank is represented as black line in (b).

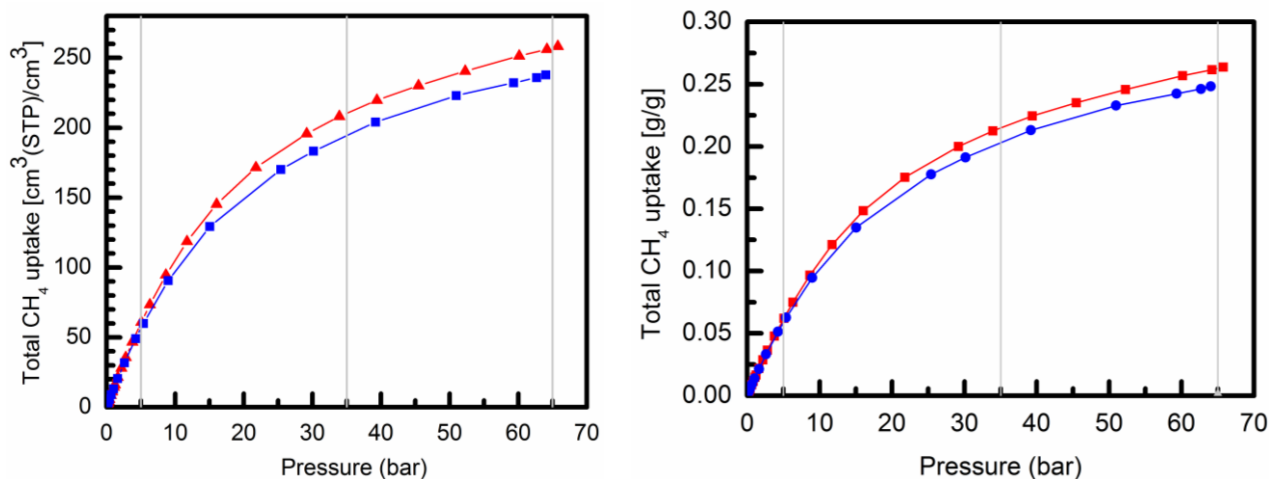


Figure S21. The comparison of the total volumetric (left) and gravimetric (right) methane uptake at 298 K of UTSA-76a (red) and NOTT-101a (blue).

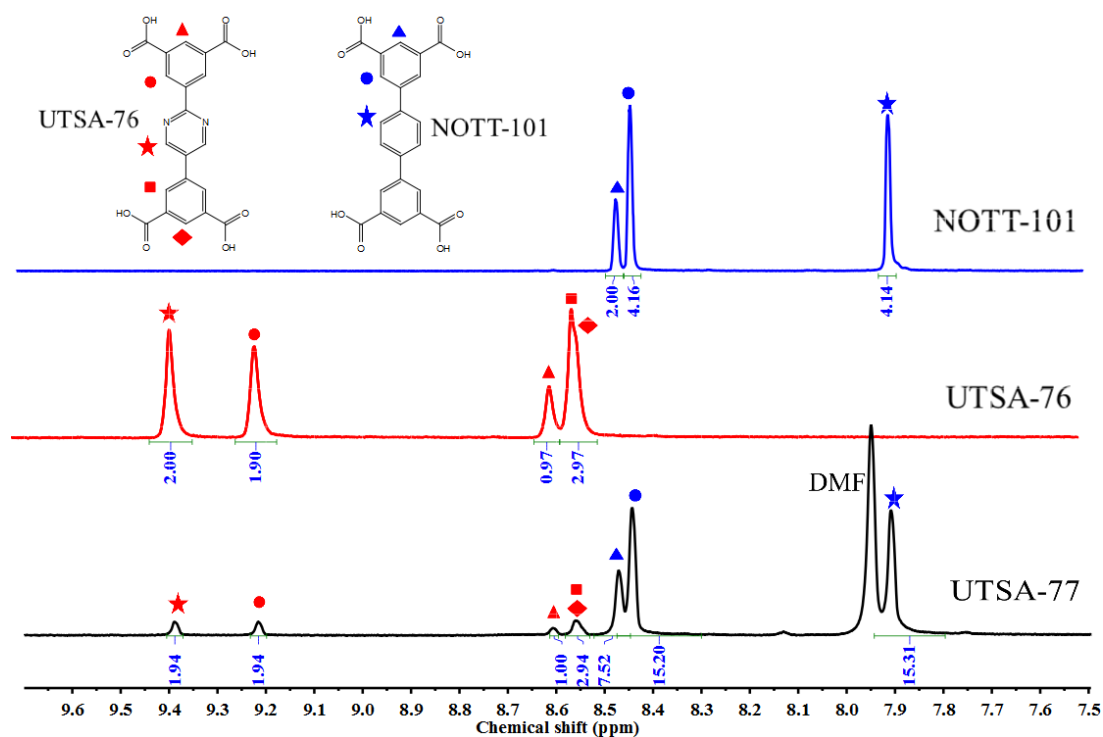


Figure S22. Comparison of ¹H (DMSO-d₆, 500MHz) spectrum of UTSA-77, UTSA-76, and NOTT-101, demonstrating the linker ratio for L1:L4 in the UTSA-77 backbone to be 4:1.

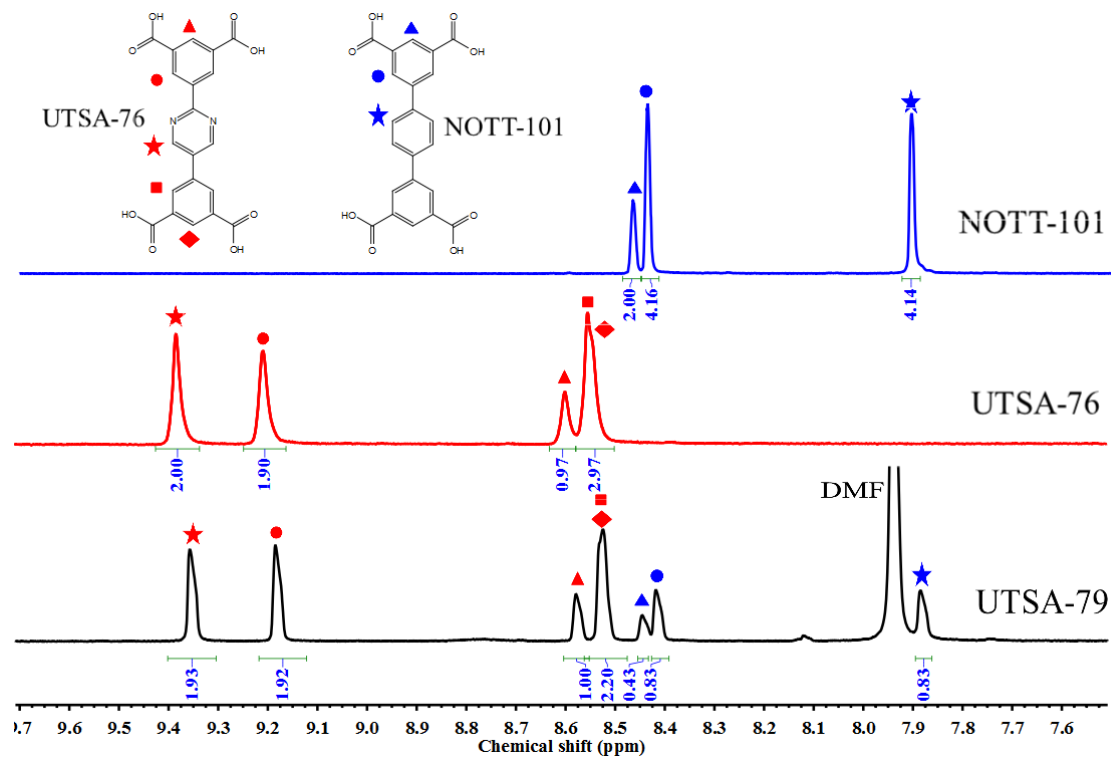


Figure S23. Comparison of ^1H (DMSO- d_6 , 500MHz) spectrum of UTSA-79, UTSA-76, and NOTT-101, demonstrating the linker ratio for L1:L4 in the UTSA-79 backbone to be 1:4.

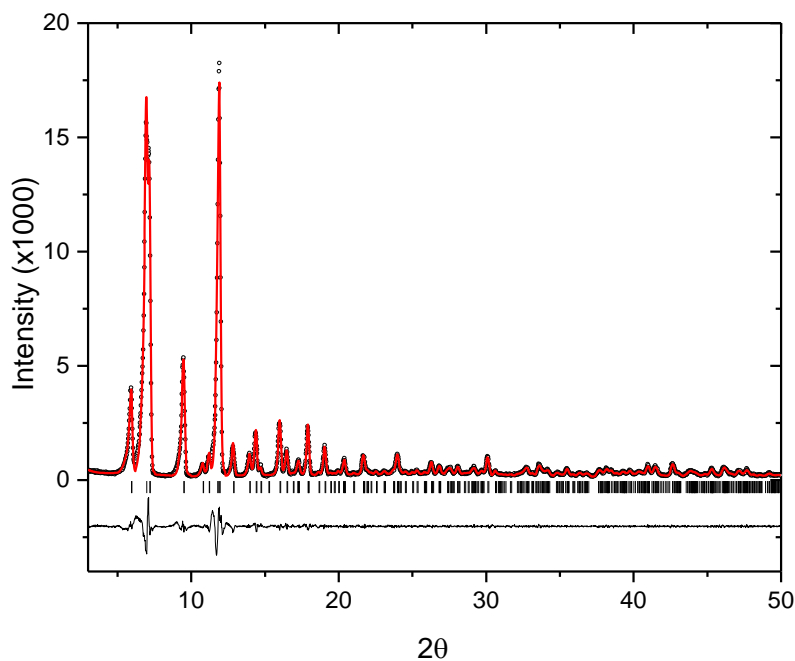


Figure 24. Experimental (circles), Le Bail fitted (line), and difference (line below observed and calculated patterns) PXRD profile for activated UTSA-75a at 298 K (Cu $K\alpha$ radiation). Vertical bars indicate the calculated positions of Bragg peaks. Refined lattice parameters: $a=18.596(1)$ Å and $c=38.007(4)$ Å. Goodness of fit: $R_p=0.0634$, $R_{wp}=0.0913$. Corresponding crystal density: 0.698 g/cc.

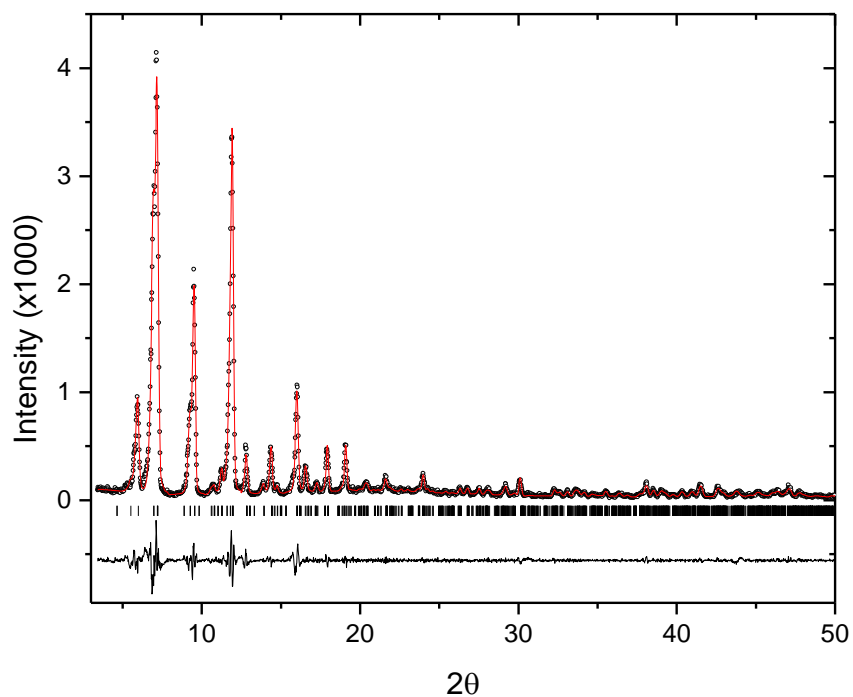


Figure S25. Experimental (circles), Le Bail fitted (line), and difference (line below observed and calculated patterns) PXRD profile for activated UTSA-78a at 298 K (Cu K α radiation). Vertical bars indicate the calculated positions of Bragg peaks. Refined lattice parameters: $a=18.581(1)$ Å and $c=38.232(5)$ Å. Goodness of fit: $R_p=0.0765$, $R_{wp}=0.0955$. Corresponding crystal density: 0.694 g/cc.

The performance limit of methane storage for MOF materials under 65 bar and room temperature

In this work, we used a series of copper–tetracarboxylate frameworks (NOTT-100, NOTT-101, NOTT-102, NOTT-103, and NOTT-109) with similar structures but systematically varied porosities to reveal the relationship between the total volumetric methane uptake (65 bar and RT) and pore volumes. Based on our previous work, there is a linear data fit between the saturated methane storage at 150 K and pore volume: $C_{\text{sat}} = -17.728 + 532.234 \times V_p$, where C_{sat} is the excess saturated methane uptake at 150 K in cm^3 (STP) g^{-1} , and V_p is the pore volume in $\text{cm}^3 \text{g}^{-1}$ (Fig. S26a).² In order to rationalize the relationship between the gravimetric methane storage under 65 bar and RT and pore volume, let us first define the pore occupancy, O , under 65 bar and room temperature, as excess methane storage amount under 65 bar and room temperature, C_{excess} , divided by excess saturated methane storage amount, C_{sat} . As shown in Fig. S26b, we found that the pore occupancy is linearly related with the corresponding pore volume: $O = 0.7332 - 0.2013 \times V_p$, where O is methane storage pore occupancy, dimensionless, and V_p is pore volume in $\text{cm}^3 \text{g}^{-1}$. The more porous the MOF is, the lower the pore occupancy is. Thus, the excess methane storage capacity (C_{excess}) of a specific MOF at RT and 65 bar can be calculated by the equation: $C_{\text{excess}} = O \times C_{\text{sat}} = (0.7332 - 0.2013 \times V_p) \times (-17.728 + 532.234 \times V_p) = -107.139 \times V_p^2 + 393.800 \times V_p - 12.998$. We further estimated the total methane storage capacity (C_{total}) at room temperature and 65 bar using the following equation: $C_{\text{total}} = C_{\text{excess}} + \text{methane density} \times 22.4 \times V_p$ (65 bar and 300 K) (cm^3/g) = $-107.139 \times V_p^2 + 458.805 \times V_p - 12.998$, where methane density at 65 bar and 300 K is 2.902 mol/L.³

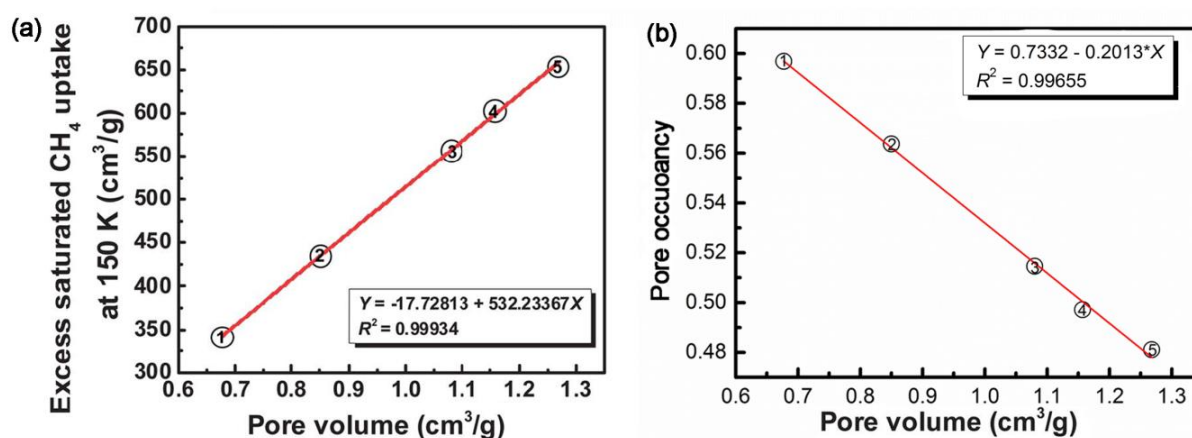


Figure S26. (a) Saturated excess gravimetric methane adsorption capacity at 150 K (cm^3 (STP) g^{-1})

versus pore volume ($\text{cm}^3 \text{g}^{-1}$) of the MOFs investigated. (b) Pore occupancy versus pore volume ($\text{cm}^3 \text{g}^{-1}$). Pore occupancy is defined as the excess gravimetric methane uptake at 300 K and 65 bar divided by the saturated excess gravimetric methane uptake at 150 K. The solid lines show the linear fitting results. 1: NOTT-100a; 2: NOTT-109a; 3: NOTT-101a; 4: NOTT-103a; 5: NOTT-102a. Fig. 26(a) was reprinted with permission from ref. 2. Copyright 2013 Royal Society of Chemistry.

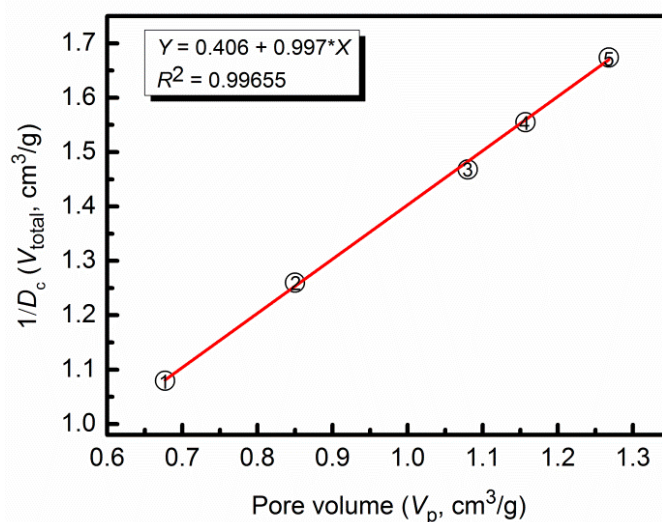


Figure S27. The $1/\text{framework density}$ (D_c , g cm^{-3}) versus the framework pore volume (V_p , $\text{cm}^3 \text{g}^{-1}$). The solid lines show the linear fitting results. 1: NOTT-100a; 2: NOTT-109a; 3: NOTT-101a; 4: NOTT-103a; 5: NOTT-102a. D_c = framework densities without guest molecules and terminal waters.

To obtain the volumetric methane storage capacity, the framework density should be taken into account (volumetric methane storage capacity = gravimetric methane storage capacity \times framework density). Using this series of MOFs, we found that $1/(\text{framework density})$ is basically linearly correlated to the pore volume of the framework: $1/D_c = 0.997 \times V_p + 0.406$, thus $D_c = 1/(0.997 \times V_p + 0.406)$ (Fig. S27). This relationship is consistent with the ones reported in previous works.^{4,5} As a result, the total volumetric methane storage capacity at 65 bar and RT can be approximately calculated by the following equation: $C_{\text{total}} \times D_c = (-107.139 \times V_p^2 + 458.805 \times V_p - 12.998)/(0.997 \times V_p + 0.406)$. The detailed comparison of the experimental total volumetric methane uptakes at room temperature and 65 bar and the ones predicted from this empirical equation in different types of MOFs is listed in Table S1. The calculated methane uptakes systematically match with the experimental methane storage ones well (the average deviation is 4.6%), suggesting that it is feasible

to predict the total volumetric methane uptake (65 bar and 300 K) of MOF materials once we establish their permanent porosities (pore volumes).

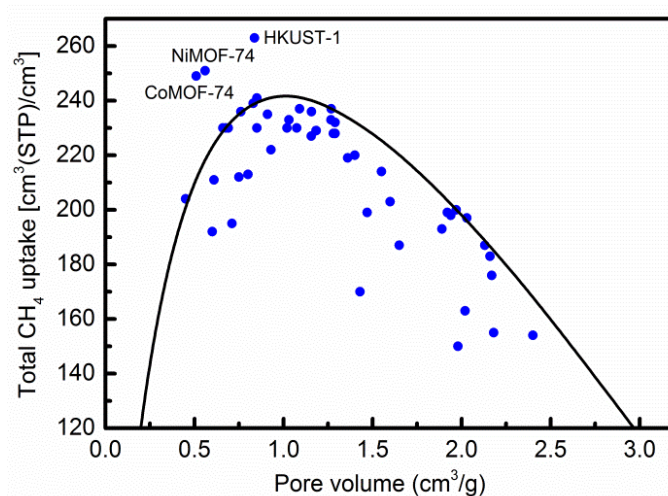


Figure S28. The plot of the predicted total volumetric methane storage capacity, (cm^3 (STP) cm^{-3}) at 65 bar and 300 K versus the framework pore volume, V_p , ($\text{cm}^3 \text{g}^{-1}$) according to the empirical equation: total volumetric uptake = $(-107.139 \times V_p^2 + 458.805 \times V_p - 12.998)/(0.997 \times V_p + 0.406)$. The inset blue points are the experimental total volumetric methane uptakes of different types of MOFs at room temperature and 65 bar (Table S1).

The plot of the predicted total volumetric methane uptake (65 bar and 300 K) versus pore volume of MOF materials is shown in Fig. S28. When the MOF pore volume increases, the total volumetric uptake at 65 bar and RT firstly increases and then decreases, displaying a performance limit for methane storage at 65 bar and RT. Almost all the reported MOFs show the volumetric methane storage near or below the performance limit. Only two types of MOFs are beyond this limit: the first one is MOFs containing exceptionally high density of OMSs, like NiMOF-74 ($7.74 \text{ mmol cm}^{-3}$), CoMOF-74 ($7.25 \text{ mmol cm}^{-3}$), and HKUST-1 ($4.40 \text{ mmol cm}^{-3}$); the other is the functionalized MOFs investigated here (Fig. S29). Despite high total capacities for NiMOF-74 (251 cm^3 (STP) cm^{-3}),⁵ CoMOF-74 (249 cm^3 (STP) cm^{-3}),⁶ and HKUST-1 (267 cm^3 (STP) cm^{-3}),⁵ the high densities of OMSs also lead to the high uptakes below 5 bar, which are 122 , 113 , and 77 cm^3 (STP) cm^{-3} , respectively. All of these values are much higher than our functionalized MOFs (ca. 60 cm^3 (STP) cm^{-3}). Thus, a comparatively poor working capacity was observed for MMOF-74.^{5,6} Although

HKUST-1 shows a relatively high working capacity ($190 \text{ cm}^3 \text{ (STP) cm}^{-3}$) due to its exceptionally high total capacity, two of our functionalized MOFs (UTSA-75a and UTSA-76a) still exhibit higher working capacities than HKUST-1. As a result, although both the above strategies are capable of improving the total volumetric methane storage capacity, the functionalized MOFs with suitable functional sites are the better choice for achieving high working capacity.

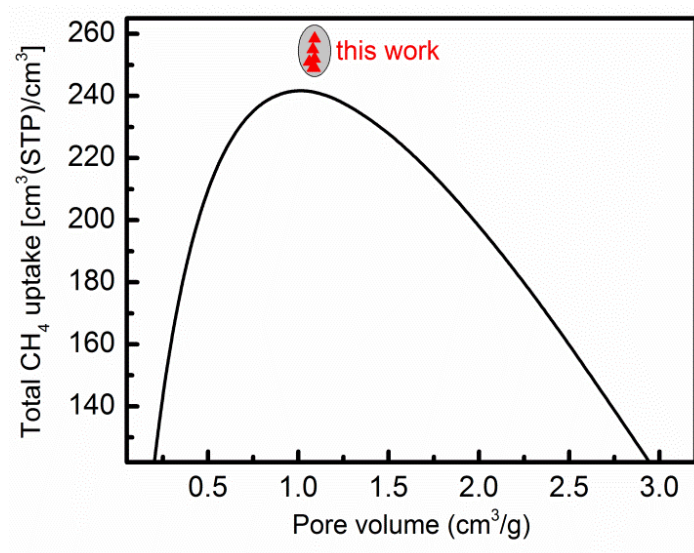


Figure S29. The plot of the total volumetric methane storage capacity, ($\text{cm}^3 \text{ (STP) cm}^{-3}$) at 65 bar and 300 K versus the framework pore volume, V_p , ($\text{cm}^3 \text{ g}^{-1}$) according to the empirical equation. The inset red triangles represent the experimental total volumetric methane uptakes at room temperature and 65 bar for the functionalized MOFs investigated here.

Table S1: Comparison of the experimental total methane uptakes at 65 bar and ambient temperature and the predicted ones according to the established empirical equation and pore volumes (the average deviation is 4.6%).

MOFs	Experimental		Predicted	Deviation (%)	Reference
	Pore volume [cm ³ /g]	Total methane uptakes [cm ³ /cm ³]	Total methane uptakes [cm ³ /cm ³]		
ZJU-5a	1.09	249	240	3.6	This work
UTSA-75a	1.06	251	241	3.9	This work
UTSA-76a	1.09	257	240	7.0	This work
UTSA-77a	1.08	249	240	3.6	This work
UTSA-78a	1.09	252	240	4.0	This work
UTSA-79a	1.08	255	240	5.9	This work
CoMOF-74	0.51	249	214	14.0	6
NiMOF-74	0.56	251	221	11.9	5
UTSA-20	0.66	230	229	0.4	5
NOTT-100a	0.677	230	231	0.4	2
MgMOF-74	0.69	230	232	0.8	6
Zn ₂ (bdc) ₂ (dabco)	0.75	235	212	9.8	7
HKUST-1	0.837	267	240	11.2	5
NOTT-109a	0.85	242	238	1.6	2
PCN-14	0.85	230	238	3.4	5
PCN-11	0.91	235	240	2.1	8
Cu-TDPAT	0.93	222	241	8.5	9
UTSA-80a	1.03	233	241	3.4	10
NOTT-101a	1.09	237	240	1.2	2
ZJU-35	1.156	227	239	5.3	4
NOTT-103a	1.157	236	239	1.2	2
ZJU-25	1.183	229	239	4.3	11
ZJNU-50a	1.184	229	239	4.3	12
NOTT-102a	1.268	237	237	0	2
NU-125	1.29	228	235	3.1	13
NU-125	1.29	232	235	1.3	5
PCN-61	1.36	219	232	5.9	14
MOF-5	1.55	214	225	5.1	6
ZJU-36	1.599	203	222	9.3	4
MOF-177	1.89	193	204	5.7	15
FJI-H5	1.92	199	203	2.0	16
NU-140	1.97	200	199	0.5	17
DUT-23(Co)	2.03	197	196	0.5	18
NU-111	2.09	206	192	6.8	19
PCN-68	2.13	187	189	1.0	14

MOF-205	2.16	183	187	2.1	15
NOTT-119	2.40	154	166	7.8	20

Table S2. Crystallographic data and structure refinement results for UTSA-75 (from single-crystal X-ray diffraction analysis on the as-synthesized sample).

UTSA-75	
Formula	C ₂₀ H ₁₂ Cu ₂ N ₂ O ₁₀
Formula weight	567.40
Temperature/K	100.00(19)
Crystal system	Trigonal
Space group	R-3m
<i>a</i> , <i>b</i> (Å)	18.7387(3)
<i>c</i> (Å)	37.4863(8)
α (°)	90.00
β (°)	90.00
γ (°)	120.00
<i>V</i> (Å ³)	11399.4(4)
<i>Z</i>	9
<i>D</i> _{calcd} (g cm ⁻³)	0.744
μ (mm ⁻¹)	1.274
<i>F</i> (000)	2556.0
Crystal size/mm ³	0.15 × 0.12 × 0.10
GOF	0.943
<i>R</i> _{int}	0.0399
<i>R</i> ₁ , <i>wR</i> ₂ [I ≥ 2σ (I)]	0.0472, 0.1035
<i>R</i> ₁ , <i>wR</i> ₂ [all data]	0.0518, 0.1019
Largest diff. peak and hole (e Å ⁻³)	0.547, -0.570

References

1. W. Zhou, H. Wu, M. R. Hartman and T. Yildirim, *J. Phys. Chem. C*, 2007, **111**, 16131–16137.
2. Y. He, W. Zhou, T. Yildirim and B. Chen, *Energy Environ. Sci.*, 2013, **6**, 2735–2744.
3. See website at <http://webbook.nist.gov/chemistry/fluid/>.
4. G.-Q. Kong, Z.-D. Han, Y. He, S. Ou, W. Zhou, T. Yildirim, R. Krishna, C. Zou, B. Chen and C.-D. Wu, *Chem.–Eur. J.*, 2013, **19**, 14886–14894.
5. Y. Peng, V. Krungleviciute, I. Eryazici, J. T. Hupp, O. K. Farha and T. Yildirim, *J. Am. Chem. Soc.*, 2013, **135**, 11887–11894.
6. J. A. Mason, M. Veenstra and J. R. Long, *Chem. Sci.*, 2014, **5**, 32–51.

7. I. Senkowska and S. Kaskel, *Microporous Mesoporous Mater.*, 2008, **112**, 108–115.
8. X.-S. Wang, S. Ma, K. Rauch, J. M. Simmons, D. Yuan, X. Wang, T. Yildirim, W. C. Cole, J. J. López, A. d. Meijere and H.-C. Zhou, *Chem. Mater.*, 2008, **20**, 3145–3152.
9. B. Li, Z. Zhang, Y. Li, K. Yao, Y. Zhu, Z. Deng, F. Yang, X. Zhou, G. Li, H. Wu, N. Nijem, Y. J. Chabal, Z. Lai, Y. Han, Z. Shi, S. Feng and J. Li, *Angew. Chem., Int. Ed.*, 2012, **51**, 1412–1415.
10. H.-M. Wen, B. Li, D. Yuan, H. Wang, T. Yildirim, W. Zhou and B. Chen, *J. Mater. Chem. A*, 2014, **2**, 11516–11522.
11. X. Duan, J. Yu, J. Cai, Y. He, C. Wu, W. Zhou, T. Yildirim, Z. Zhang, S. Xiang, M. O’Keeffe, B. Chen and G. Qian, *Chem. Commun.*, 2013, **49**, 2043–2045.
12. C. Song, Y. Ling, Y. Feng, W. Zhou, T. Yildirim and Y. He, *Chem. Commun.*, 2015, **51**, 8508–8511.
13. C. E. Wilmer, O. K. Farha, T. Yildirim, I. Eryazici, V. Krungleviciute, A. A. Sarjeant, R. Q. Snurr and J. T. Hupp, *Energy Environ. Sci.*, 2013, **6**, 1158–1163.
14. D. Yuan, D. Zhao, D. Sun and H.-C. Zhou, *Angew. Chem., Int. Ed.*, 2010, **49**, 5357–5361.
15. H. Furukawa, N. Ko, Y. B. Go, N. Aratani, S. B. Choi, E. Choi, A. Ö. Yazaydin, R. Q. Snurr, M. O’Keeffe, J. Kim and O. M. Yaghi, *Science*, 2010, **329**, 424–428.
16. J. Pang, F. Jiang, M. Wu, D. Yuan, K. Zhou, J. Qian, K. Su and M. Hong, *Chem. Commun.*, 2014, **50**, 2834–2836.
17. G. Barin, V. Krungleviciute, D. A. Gomez-Gualdron, A. A. Sarjeant, R. Q. Snurr, J. T. Hupp, T. Yildirim and O. K. Farha, *Chem. Mater.*, 2014, **26**, 1912–1917.
18. N. Klein, I. Senkowska, I. A. Baburin, R. Grünker, U. Stoeck, M. Schlichtenmayer, B. Streppel, U. Mueller, S. Leoni, M. Hirscher and S. Kaskel, *Chem.–Eur. J.*, 2011, **17**, 13007–13016.
19. Y. Peng, G. Srinivas, C. E. Wilmer, I. Eryazici, R. Q. Snurr, J. T. Hupp, T. Yildirim and O. K. Farha, *Chem. Commun.*, 2013, **49**, 2992–2994.
20. Y. Yan, S. Yang, A. J. Blake, W. Lewis, E. Poirier, S. A. Barnett, N. R. Champness and M. Schröder, *Chem. Commun.*, 2011, **47**, 9995–9997.